J Genet Resour2026; 12(2): 180-194 *Homepage: http://sc.journals.umz.ac.ir/*

RESEARCH ARTICLE *DOI: 10.22080/jgr.2026.32074.1467*

J|G|R

Glucose-functionalized Iron Oxide Nanoparticles Which Co-conjugated with Hyaluronic Acid and Naringenin Induces ROS-mediated Apoptosis and Cell Cycle Arrest in Colon Cancer Cells

Yaser Mohammadi[1], Fariba Sharifnia[1]*, Monireh Movahedi[1] and Ali Salehzadeh[2]

[1] Department of Biochemistry, NT.C., Islamic Azad University, Tehran, Iran
[2] Department of Biology, Ra.C., Islamic Azad University, Rasht, Iran

ARTICLE INFO

Article history:
Received 01 June 2026
Accepted 02 July 2026
Available 20 July 2026

Keywords:
Apoptosis
Caspase-8 upregulation
Flow cytometry
Hyaluronic acid
Naringenin
Targeted drug delivery

Corresponding authors:
✉ F. Sharifnia
fa.sharifnia@iau.ac.ir

p-ISSN 2423-4257
e-ISSN 2588-2589

ABSTRACT

Targeted drug delivery has received attention in cancer chemotherapy. In the present study, glucose (Glu)-functionalized iron oxide nanoparticles (Fe_3O_4 NPs) were co-conjugated with hyaluronic acid (HA) and naringenin (NAR), and their anticancer potential against colon cancer cells was characterized. Properties of Fe_3O_4@Glu-HA-NAR NPs were investigated by SEM, DLS, zeta potential, FT-IR, and XRD analyses. Cytotoxicity of the NPs in HT-116 and HDF cell lines was investigated by an MTT assay. The effects of the Fe_3O_4@Glu-HA-NAR NPs on cell cycle and apoptosis/necrosis in HT-116 cell line was studied by flow cytometry. AO/PI staining and real-time PCR were employed to evaluate nuclear morphology and expression of caspase-8 gene in the cancer cells, and reactive oxygen species (ROS) levels were also determined. The Fe_3O_4@Glu-HA-NAR NPs exhibited spherical to cubic morphology, an average particle size of 77.6 nm, surface charge of -57.9 mV, hydrodynamic size of 783 nm, and structural characteristics similar to their constituent components. Fe_3O_4@Glu-HA-NAR nanoparticles demonstrated concentration-dependent cytotoxicity toward the studied cells with greater toxicity against HT-116 cells [50% inhibitory concentration (IC_{50}) = 42.63 µg/mL]. In comparison, free NAR exhibited a higher IC_{50} value (64.62 µg/mL), indicating that nanoparticle-mediated delivery enhanced the antiproliferative efficacy of NAR against colon cancer cells. Treatment of the HT-116 cells with Fe_3O_4@Glu-HA-NAR NPs blocked cell cycle progression at the S and G2/M phases, elevated cell necrosis and late apoptosis and caused nuclear alterations, including chromatin condensation. Exposure to Fe_3O_4@Glu-HA-NAR significantly upregulated the expression of the *CASP-8* gene (3.8-fold) and increased ROS levels by 13.0-fold. This study demonstrates the promising potential of Fe_3O_4@Glu-HA-NAR NPs in targeting colon cancer cells.

Please cite this paper as: Mohammadi, Y., Sharifnia, F., Movahedi, M., & Salehzadeh, A. (2026). Glucose-functionalized iron oxide nanoparticles which co-conjugated with hyaluronic acid and naringenin induces ROS-mediated apoptosis and cell cycle arrest in colon cancer cells. *Journal of Genetic Resources,* 12(2), 180-194. doi: 10.22080/jgr.2026.32074.1467

Introduction

Targeted drug delivery is an innovative chemotherapy approach that has received much attention recently in cancer treatment. Owing to the metabolic and functional differences between cancer and normal cells, targeted drug delivery enables the selective delivery of therapeutic agents to tumor tissues. This approach reduces drug distribution to non-target tissues, thereby enhancing the effectiveness of chemotherapy while minimizing its adverse side effects (Sharma *et al.,* 2024).

Iron oxide nanoparticles (IONPs) exhibit several advantages such as superparamagnetism, large surface area, as well as rapid and easy separation from solution under an external magnetic field. Therefore, IONPs have been extensively studied and applied in biomedicine (Gambhir *et al.,* 2022). The magnetic property of IONPs provides

an efficient and stable method of drug delivery using an external magnetic field. IONPs are stable, inexpensive to produce, biocompatible, and can provide controlled and sustained drug release through surface manipulation (Stanicki *et al.*, 2022). For these reasons, IONPs have received increasing attention in cancer diagnosis and treatment.

Hyaluronic acid (HA) is an extracellular polysaccharide made up of subunits of D-glucuronic acid and N-acetyl-D-glucosamine that is abundantly found in the human extracellular matrix and connective tissue (Fu *et al.,* 2023). It has been found that HA can play several roles in cell proliferation and tissue regeneration. Upon attachment to its cell surface receptor, CD44, HA enhances downstream signaling pathways related to proliferation, invasion, and metastasis in cancer cells. Since HA receptors are usually overexpressed in cancer cells, HA-containing drugs can selectively bind to cancer cells and facilitate drug delivery to the cells, leading to increased drug absorption in cancer cells and reduced side effects in healthy cells (Fu *et al.,* 2023; Jia *et al.,* 2022; Heydari *et al.*, 2024).

Phytochemical bioactive compound have various biomedical properties, such as antioxidant, anti-inflammatory, antimicrobial, and antitumor activities (de Luna *et al.,* 2023). Naringenin and naringin are the main bioactive flavonoids in citrus fruits and are known for their beneficial effects on human health. Research has shown that plant flavonoids can be used to promote cancer cell death and inhibit cell proliferation and metastasis. It was reported that NAR and naringin exhibit anticancer potential through modulation of several signaling pathways such as NF-κB, p38/MAPK, and activation of caspases, leading to the suppression of cell growth and apoptosis induction (Rauf *et al.,* 2022; Stabrauskiene *et al.,* 2022). Furthermore, it has been documented that NAR can promote pro-apoptotic genes, attenuate cyclin-dependent kinases and regulate the genes associated with the P53 signaling pathway in colorectal cancer cells (Zamanian *et al.,* 2024). Wang *et al.* (2024) reported that NAR can reduce the viability of colorectal cancer cells through apoptosis induction, and significantly promote the anticancer effects of 5-fluorouracil (5-FU). They reported that NAR in combination with 5-FU alters mitochondrial function by increasing ROS levels and decreasing the mitochondrial membrane potential, leading to stimulation of AMPK/mTOR signaling and apoptosis induction. Therefore, targeting cancer cells with NAR could be a promising approach in cancer treatment.

With an estimated annual 1.15 and 0.58 million new cases and deaths, colon cancer is considered the fifth most frequent cause of cancer-related mortality in the human population worldwide (Sung *et al.,* 2021). Surgery to remove tumor tissues is considered the first-line treatment for colon cancer. However, adjuvant chemotherapy is the most important post-surgery option to prevent recurrence and metastasis of colon cancer (Oki *et al.,* 2022). In recent years, research studies focused on designing and characterizing novel anticancer agents against this disease have become a major constant priority. Considering the potential of nanomedicines in cancer treatment, this study aimed to synthesize glucose-functionalized iron oxide nanoparticles co-conjugated with HA and NAR (Fe_3O_4@Glu-HA-NAR NPs) and characterize their anticancer potential and underlying mechanism in colon cancer cells.

Materials and Methods

Synthesis of Fe_3O_4@Glu-HA-NAR NPs

Fe_3O_4 nanoparticles (Fe_3O_4 NPs) were purchased from US Research Nanomaterials (USA). To facilitate the conjugation of hyaluronic acid (HA) and NAR, the Fe_3O_4 NPs were first functionalized with D-glucose (Glu). Briefly, 1.0 g of Fe_3O_4 NPs and 0.5 g of D-glucose were dispersed in 60 mL of distilled water and sonicated for 30 min to obtain a homogeneous suspension. The mixture was then transferred into a 100 mL Teflon-lined stainless-steel autoclave and heated at 180 °C for 3 h. After cooling to room temperature, the Fe_3O_4@Glu nanoparticles were collected by centrifugation at 6000 rpm, washed three times with distilled water and ethanol to remove unreacted materials, and dried at 60 °C for 5 h.

For the preparation of Fe_3O_4@Glu-HA-NAR nanoparticles, 0.5 g of Fe_3O_4@Glu nanoparticles, 0.1 g of hyaluronic acid, and 0.5 g of NAR were

dispersed in 50 mL of distilled water using ultrasonic treatment. The suspension was then incubated in a shaker incubator under continuous agitation at room temperature for 24 h to facilitate conjugation. Subsequently, the nanoparticles were collected by centrifugation at 6000 rpm, washed three times with distilled water to remove unbound HA and NAR, and finally freeze-dried for 24 h to obtain the Fe_3O_4@Glu-HA-NAR nanoparticles (Kazemzadeh et al., 2026).

Characterization of Fe3O4@Glu-HA-NAR NPs

Morphological characteristics of the NPs were investigated by Scanning Electron Microscopy (TESCAN Mira3 SEM), followed by an EDS-mapping assay to elucidate the elemental composition of the particles. The zeta potential and particle diameter in an aqueous medium were measured using a Malvern Ltd 6.32 instrument. FT-IR analysis was performed using a Nicolet IR-100 FT-IR device and the crystal structure of the NPs was studied by an XRD analysis (Co-Ka X-radiation, λ= 1.79 Å).

Cell culture

The HT-116 colon cancer and the HDF normal cell line were obtained from the Pasteur Institute of Iran. The cells were grown in RPMI-1640 medium at 37 °C with 5% CO_2.

Cell viability assay

The viability levels of the colon cancer and normal cells after a 24-hour exposure to different concentrations of Fe_3O_4@Glu-HA-NAR NPs and free NAR were examined by an MTT assay. The cells were propagated in the RPMI-1640 medium; their density was adjusted to 1×10^4 cells/mL and seeded into a 96-well plate containing a gradient concentration of the NPs (10, 20, 40, 80 and 160 µg/mL). The untreated cells were served as controls. The cells were incubated for 24 hours, and next, subjected to an MTT assay. Briefly, 0.2 mL of MTT solution (2-(4,5-dimethylthiazol-2-yl) -2,5-diphenyltetrazolium bromide) was added to the wells and incubated for 4 hours at 37°C. After aspiration of medium, 0.2 mL of DMSO solution was added. Following incubation for 30 min at room temperature, the absorbance was measured at 570 nm. The following equation was used to determine the inhibition percentage in each well (Hosseinkhah *et al.,* 2022; Kumari *et al.,* 2020):
Inhibition percentage= (OD570 of untreated wells- OD570 of treated wells)/ OD570 of untreated wells× 100.

Flow cytometry analysis

Flow cytometry assay was employed to examine the effects of Fe_3O_4@Glu-HA-NAR NPs on the cell cycle of cancer cells. The HT-116 cells were initially treated with the NPs at their IC_{50} for 24 hours. Next, the cells were stained with propidium iodide (PI) and treated with RNase A (BioLegend) to remove their RNA content. Finally, a flow cytometry analysis (ZE5, Bio-Rad) was utilized to evaluate the cell cycle phases of cancer cells.
To determine the cell apoptosis/necrosis levels, the HT-116 cells were treated with Fe_3O_4@Glu-HA-NAR NPs, as described above, and then stained with propidium iodide (PI) and Annexin V (BioLegend, USA). Finally, cell apoptosis/necrosis levels were analyzed using flow cytometry.

Acridine orange/propidium iodide (AO/PI) staining

The HT-116 cells were subjected to AO/PI staining to examine the cellular and nuclear morphology. In brief, the cells were treated with Fe_3O_4@Glu-HA-NAR NPs, as described above. Next, Acridine Orange and propidium iodide solutions (Sigma-Aldrich) were used to stain the treated and control cells. Finally, the cellular and nuclear morphology of the cells was studied under a fluorescence microscope (Ramezani *et al.,* 2019).

Expression of CASP-8

The expression of the caspase-8 gene (*CASP-8*) was studied using real-time PCR assay. After treatment of the HT-116 cells with Fe_3O_4@Glu-HA-NAR NPs, cellular RNA content was extracted using the Yekta Tajhiz (Iran) kit, according to the manufacturer's instruction. The cDNA was synthesized using the Yekta Tajhiz (Iran) kit, and gene-specific primers were used to amplify the DNA fragments using a SYBR-Green real-time PCR master mix (Yekta Tajhiz, Iran). The *GAPDH* was used as the internal

reference gene for normalization because previous studies have demonstrated its stable expression in colorectal cancer cells under comparable experimental conditions (Ahmadzadeh Chaleshtori *et al*., 2025) and gene expression level was calculated using the $2^{-\Delta\Delta CT}$ formula (Pfaffl *et al.,* 2001). The following primers were used in this work: *GAPDH* F: 5′-GTCTCCTCTGACTTCAACAGCG-3′; *GAPDH* R: 5′-ACCACCCTGTTGCTGTAGCCAA-3′; *CASP-8* F: 5′-AGAAGAGGGTCATCCTGGGAGA-3′; *CASP-8* R: 5′-TCAGGACTTCCTTCAAGGCTGC-3′.

ROS levels

To determine the ROS levels, the HT-116 cells were initially treated with Fe_3O_4@Glu-HA-NAR NPs and then subjected to 2',7'-dichlorodihydrofluorescein (H_2DCF) (Sigma-Aldrich) for 60 min. Finally, the fluorescent emission intensity corresponds to the ROS level was quantified. The untreated cancer cells were considered the controls.

Statistical analysis

Statistical analyses were performed using SPSS version 22.0 (IBM Corp., Armonk, NY, USA). Data are presented as the mean ± standard deviation (SD) of three technical replicates. Statistical differences among groups were analyzed using one-way analysis of variance (ANOVA) followed by Tukey's post hoc multiple comparison test. A p-value < 0.05 was considered statistically significant.

Results

Characteristics of the NPs

Morphological characterization of the dried Fe_3O_4@Glu-HA-NAR NPs displayed that the NPs are spherical and partially cubic in shap; their size ranges from 25.7 to 120.0nm, and the particle size is 77.6 nm (Fig. 1).

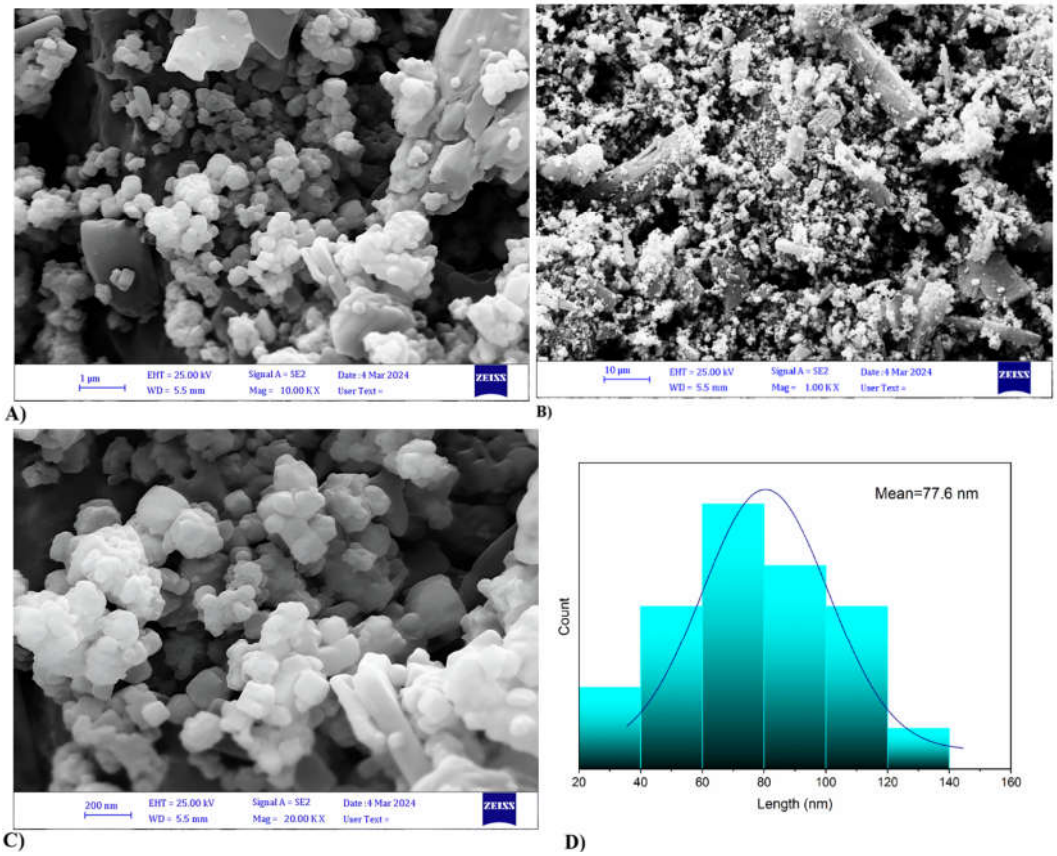

Fig. 1. FE-SEM images and size distribution of the Fe_3O_4@Glu-HA-NAR NPs. FE-SEM micrographs at different magnifications: A) 1 µm scale bar; B) 10 µm scale bar; C) 200 nm scale bar, showing spherical to cubic morphology with particle diameter ranging from 25.7 to 120 nm. D) Size distribution histogram of Fe_3O_4@Glu-HA-NAR NPs with a mean particle size of 77.6 nm.

The elemental constituents of the NPs include Fe, C and O with a weight percentage of 68.6, 20.9 and 10.6%, respectively, with no detectable elemental impurities. The elemental composition determined by EDS is semi-quantitative and reflects the surface composition of the nanocomposite. Therefore, deviations from the theoretical stoichiometric composition are expected due to the dominance of the Fe_3O_4 core, the relatively thin organic coating (glucose, HA, and NAR), and the limited accuracy of EDS for light elements. Nevertheless, the presence of Fe, C, and O without detectable impurities confirmed the successful synthesis of the Fe_3O_4@Glu-HA-NAR nanocomposite (Fig. 2).

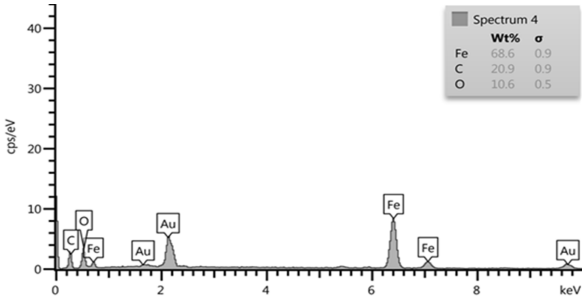

Fig. 2. Energy Dispersive X-ray Spectroscopy (EDS) analysis of Fe_3O_4@Glu-HA-NAR NPs. The EDS spectrum confirmed the presence of three elements: iron (Fe), carbon (C), and oxygen (O), with weight percentages of 68.6%, 20.9%, and 10.6%, respectively, with no detectable elemental impurities, confirming the purity of the synthesized nanoparticles.

The surface charge of the particles in an aqueous medium was -57.9 mV, and the hydrodynamic size was 783 nm with PDI equal to 0.4. The increased size of the NPs can be related to water absorption and particle aggregation in an aqueous medium (Fig. 3a and b).

In the FT-IR spectrum of Fe_3O_4, the strong absorption peaks at 410, 576 cm^{-1} are due to Fe-O bonds of Fe^{2+} and Fe^{3+} ions in octahedral sites and Fe^{3+} ion located in tetrahedral site, which indicates of the formation of Fe_3O_4 structure. The results are in agreement with previous reports, indicating correct synthesis of the NPs (Esfahani *et al.,* 2024).

In the FTIR spectrum of HA, the peaks at 1036, 1228, 1380 and 1746 cm^{-1} are related to the C-O, C=O, C-O-H, C-O bonds, respectively. Also, the absorption spectrum at 2950 cm^{-1} is related to the C-H bond and the observed peak at 3421 cm^{-1} is also related to O-H and N-H bonds (de Souza *et al.,* 2025). In the FTIR spectrum of NAR, the presence of the peaks at 815 and 1050 cm^{-1} are related to the C-H and C-O bonds, and the observed peaks at 1637 and 1453 cm^{-1} are related to the C=O and C-C bonds, respectively. The absorption spectrum at 2925 cm^{-1} is also related to the C-H bond and O-H bond, which resulted in a peak at 3412 cm^{-1} (Xie *et al.,* 2024).

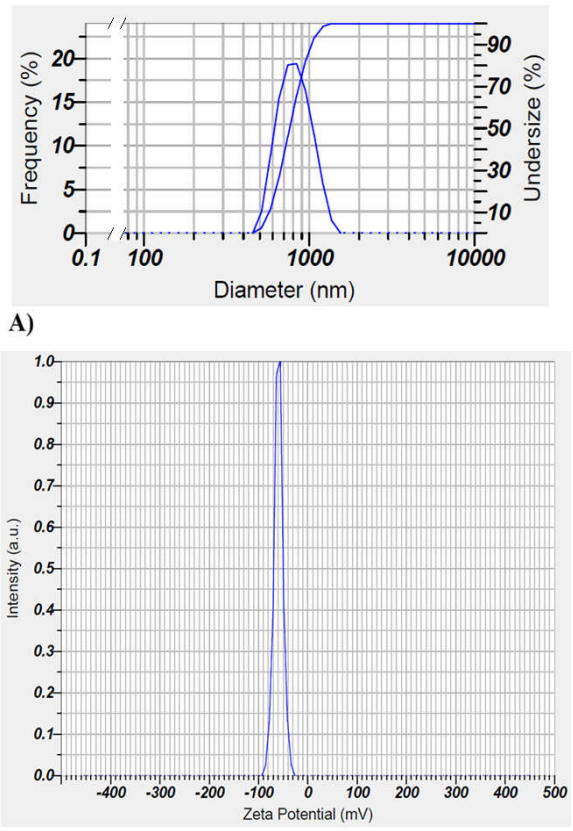

Fig. 3. Dynamic Light Scattering (DLS) and zeta potential analyses of Fe_3O_4@Glu-HA-NAR NPs: A) DLS size distribution profile showing a hydrodynamic diameter of 783 nm. The increased hydrodynamic size compared to the dry state may be attributed to water absorption and particle aggregation in aqueous medium; B) Zeta potential distribution showing a surface charge of -57.9 mV, indicating high colloidal stability of the nanoparticles in an aqueous suspension.

In the spectrum related to Fe_3O_4@Glu-HA-NAR, the presence of a peak at 583 cm^{-1} is related to the Fe-O bond, and the peaks at 801, 1185, 1376 and 1631 cm^{-1} are related to the presence of

C=C, C-O, C-H and C=O bonds, respectively. Also, the absorption peak at 2930 cm^{-1} is related to the C-H bond. The spectrums at 3450 and 3770cm^{-1} are also related to the O-H and N-H bonds, respectively. The presence of the peaks related to the constituent materials in the composite structure, suggests that the NPs have been synthesized successfully (Fig 4a).

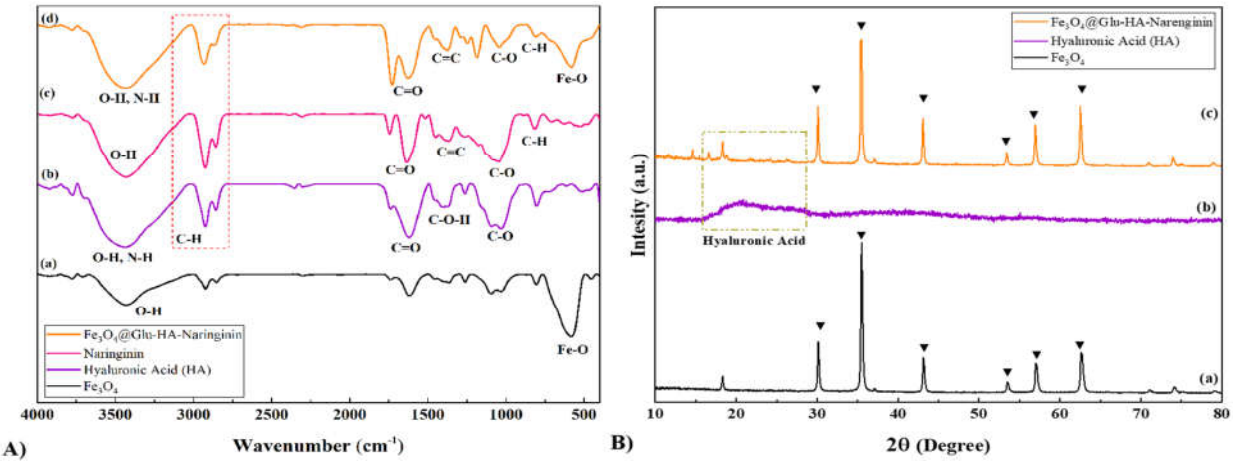

Fig. 4. FT-IR and XRD analyses of Fe_3O_4@Glu-HA-NAR NPs and their constituent materials: A) FT-IR spectra of (a) Fe_3O_4, (b) Hyaluronic acid (HA), (c) NAR, and (d) Fe_3O_4@Glu-HA-NAR NPs. The characteristic absorption peaks of Fe-O bond (583 cm^{-1}), C=C (801 cm^{-1}), C-O (1185 cm^{-1}), C-H (1376 cm^{-1}), C=O (1631 cm^{-1}), C-H (2930 cm^{-1}), and O-H/N-H bonds (3450 and 3770 cm^{-1}) in the composite spectrum confirm the successful incorporation of all constituent materials. B) XRD patterns of (a) Fe_3O_4, (b) Hyaluronic acid (HA), and (c) Fe_3O_4@Glu-HA-NAR NPs. The characteristic diffraction peaks of Fe_3O_4 at 2θ = 30.09°, 35.58°, 43.09°, 49.53°, 56.96°, and 62.52°, along with the amorphous broad peaks between 10-30° attributed to HA, confirm the successful synthesis of the nanocomposite structure.

According to the XRD pattern of Fe_3O_4, the peaks at 2θ of 30.12°, 35.5°, 43.12°, 53.49°, 57.13°, and 62.62° correspond to the iron oxide nanoparticles, which are in accordance with card number 03-0863 from the JCPDS database and consistent with previous reports (Najafipour *et al.,* 2025).

According to the intensity of the peaks in this spectrum, it can be said that the material has a high crystallinity. Also, the size of the nanoparticles from the Scherrer relation is 3.45 nm. The XRD pattern of HA displays the amorphous nature of the material, and no sharp peaks are observed in the spectrum. The presence of peaks at 2θ between 15 and 30 degrees is related to the HA material and is in accordance with the previous studies (Yilmaz *et al.,* 2024). In the spectrum of Fe_3O_4@Glu-HA-NAR, peaks at 2θ values of 30.09°, 35.58°, 43.09°, 49.53°, 56.96°, and 62.52° indicate the presence of Fe_3O_4, while the amorphous peaks at 2θ between 10° and 30° are attributed to HA in the structure. The structure of the composite is similar to that of its constituent materials. In the XRD patterns of the composite (Fig. 4b), the peak intensities are low and some peaks are absent. As a result, the crystallinity of the composite has been reduced compared to pure Fe_3O_4 (Kazemzadeh *et al.,* 2026).

The loading efficiency of NAR on Fe_3O_4@Glu-HA nanoparticles were determined by measuring the concentration of free NAR remaining in the supernatant after centrifugation using UV/Vis spectroscopy. The loading efficiency was 75%, indicating efficient incorporation of NAR into the nanoparticle formulation.

Cell viability

The viability assay demonstrated that both free NAR and Fe_3O_4@Glu-HA-NAR nanoparticles inhibited HT-116 cell proliferation in a concentration-dependent manner (Fig. 5). However, the nanoparticle formulation exhibited greater antiproliferative activity than free NAR. The IC_{50} value of free NAR against HT-116 cells was 64.62 µg/mL, whereas Fe_3O_4@Glu-HA-NAR nanoparticles showed a lower IC_{50} value of 42.63 µg/mL, indicating enhanced cytotoxic

efficacy following nanoparticle formulation. These findings suggest that conjugation of NAR to HA-functionalized iron oxide nanoparticles improves its anticancer activity against colon cancer cells. In addition, the NPs exhibited higher toxicity in the HT-116 cells than in HDF cell line. The IC_{50} of Fe_3O_4@Glu-HA-NAR NPs for normal cells was 83.85 µg/mL.

Cell apoptosis/necrosis levels

The results indicated that exposure of colon cancer cells to Fe_3O_4@Glu-HA-NAR NPs cause an increase in cell necrosis and late apoptosis and a slight increase in early apoptosis. The percentage of cell necrosis, late apoptosis and primary apoptosis increased from 3.71%, 1.03%, and 0.17% in the control cells to 15.65%, 13.14% and 0.33% in treated cells (Fig. 6).

Cell cycle analysis

According to the flow cytometry assay, the percentage of cells arrested at the S and G2/M phases considerably increased in the cancer cells treated with Fe_3O_4@Glu-HA-NAR NPs. Treatment of the HT-116 cells with the NPs increased the percentage of the cells arrested at the S and G2/M phases from 10.4% and 17.7% to 25.1% and 25.6%, respectively. In addition, the percentage of cells arrested at the G0/G1 phase dropped from 69.4% to 50.1% after exposure to the NPs (Fig. 7).

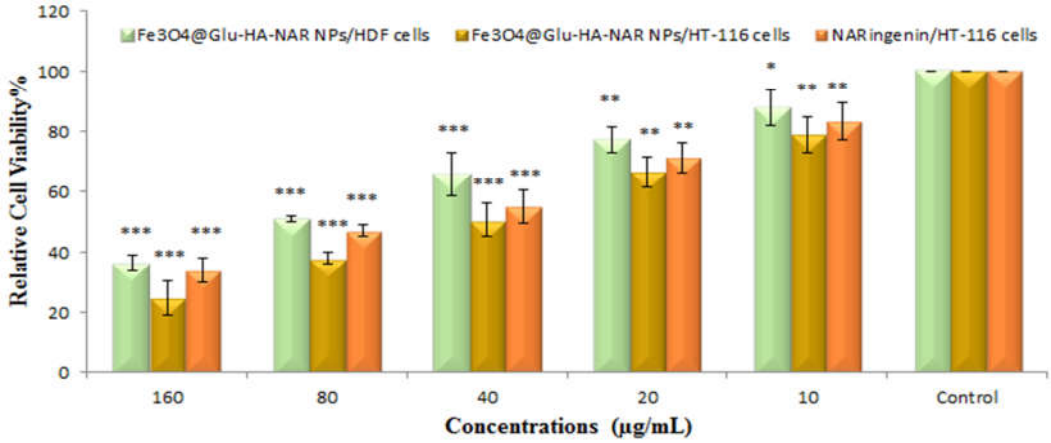

Fig. 5. Antiproliferative effects of Fe_3O_4@Glu-HA-NAR nanoparticles and free NAR (positive control) on HT-116 and HDF cells determined by the MTT assay after 24 h of treatment. The IC_{50} values of Fe_3O_4@Glu-HA-NAR nanoparticles for HT-116 and HDF cells were 42.63 and 83.85 µg/mL, respectively, while the IC_{50} value of free NAR for HT-116 cells was 64.62 µg/mL. Statistical significance was determined compared with untreated control cells, with significant differences at $p^* < 0.05$, $p^{**} < 0.01$, and $p^{***} < 0.001$.

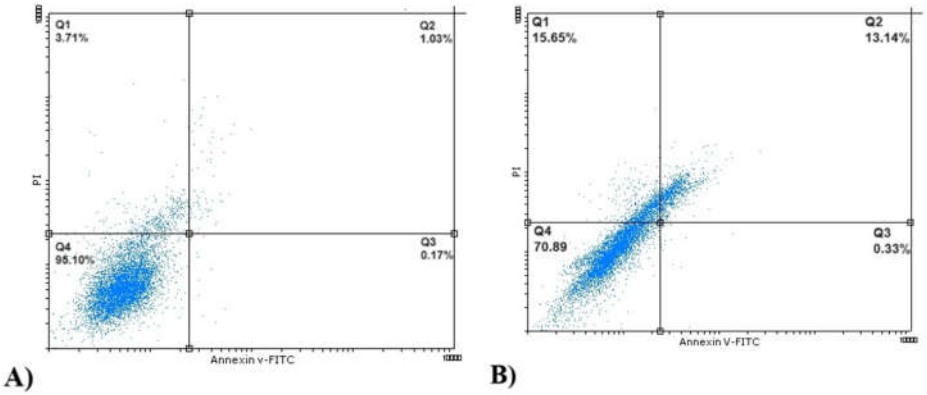

Fig. 6. Flow cytometry analysis of apoptosis and necrosis in HT-116 cells: A) Annexin V/PI dot plot of control cells showing high cell viability (Q4: 95.10%) with minimal necrosis (Q1: 3.71%) and late apoptosis (Q2: 1.03%); B) Annexin V/PI dot plot of Fe_3O_4@Glu-HA-NAR NPs-treated cells showing increased necrosis (Q1: 15.65%) and late apoptosis (Q2: 13.14%), alongside reduced cell viability (Q4: 70.89%), indicating significant induction of cell death (Q1: necrosis, Q2: late apoptosis, Q3: early apoptosis, Q4: viable cells).

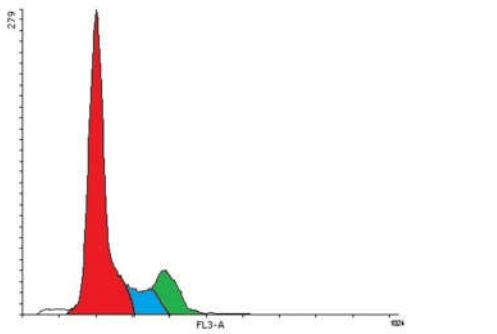

	Events	% of Vis	Mean	GeoMean	Median	CV
All events	9550	100	245.2919	232.7016	211	34.8845
SubG1	164	1.717277	84.02439	81.49505	84	24.02938
G0/G1	6635	69.47644	202.044	201.0138	202	9.985162
S	1002	10.49215	288.3303	287.4608	285	7.805296
G2/M	1693	17.72775	391.9711	390.4478	389	8.943768

A)

	Events	% of Vis	Mean	GeoMean	Median	CV
All events	8855	100	271.7683	261.6111	253	29.00148
SubG1	34	0.383964	102.3529	99.9351	99	20.83212
G0/G1	4439	50.12987	210.4485	209.5203	204	9.490529
S	2225	25.12705	288.3703	287.5571	286	7.545081
G2/M	2092	23.62507	375.7309	374.6747	375	7.776495

B)

Fig. 7. Cell cycle distribution analysis in HT-116 cells: A) Cell cycle distribution profile of control cells showing the baseline percentages of cells in the G0/G1 (69.4%), S (10.4%), and G2/M (17.7%) phases; B) Cell cycle distribution profile of Fe_3O_4@Glu-HA-NAR NPs-treated cells showing a marked reduction in the G0/G1 phase (50.1%) alongside an accumulation in the S (25.1%) and G2/M (25.6%) phases, indicating cell cycle arrest at the S and G2/M phases.

AO/PI staining

Following the treatment of colon cancer cells with Fe_3O_4@Glu-HA-NAR NPs, nuclear alterations, including chromatin condensation, nuclear fragmentation and morphological characteristics associated with apoptosis (yellow to red fluorescence) were evident in treated cells. In the control group, the healthy cells exhibited green fluorescence, indicating no significant alterations (Fig. 8).

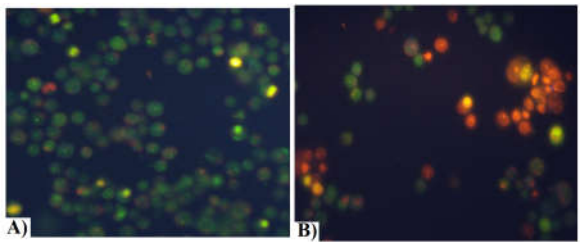

Fig. 8. AO/PI staining of colon cancer cells: A) Control; B) Cells treated with Fe_3O_4@Glu-HA-NAR NPs. Nuclear alterations, including chromatin coagulation and nuclear migration, were observed in the treated cells. Apoptosis induction and cell death are identified by a yellow to red color.

Expression of CASP-8

Treatment of HT-116 cells with Fe_3O_4@Glu-HA-NAR NPs significantly elevated the expression of the *CASP-8* gene. The *CASP-8* gene was induced by 3.8-fold following exposure to the NPs (Fig. 9).

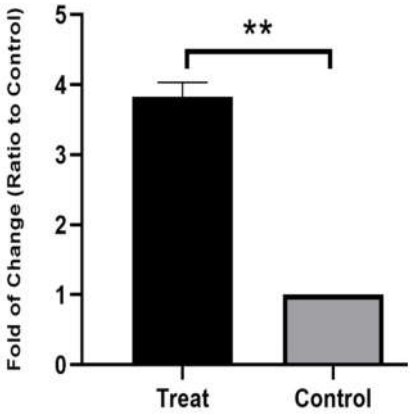

Fig. 9. Relative expression of *CASP-8* gene in HT-116 cells treated with Fe_3O_4@Glu-HA-NAR NPs compared to untreated control cells. Treatment with the NPs resulted in a 3.8-fold upregulation of *CASP-8* gene expression, indicating activation of extrinsic apoptotic pathway. Data are presented as mean± SD of three independent experiments. Significant difference at $p< 0.01$ is indicated by **.

ROS levels

Treatment with Fe_3O_4@Glu-HA-NAR NPs caused a remarkable increase in ROS generation in HT-116 cells. According to the results, the mean fluorescence intensity (MFI) in the control and treated groups was 7.17 and 93.3, respectively, indicating an elevation of 13.0-fold in ROS levels following exposure to the NPs (Fig. 10).

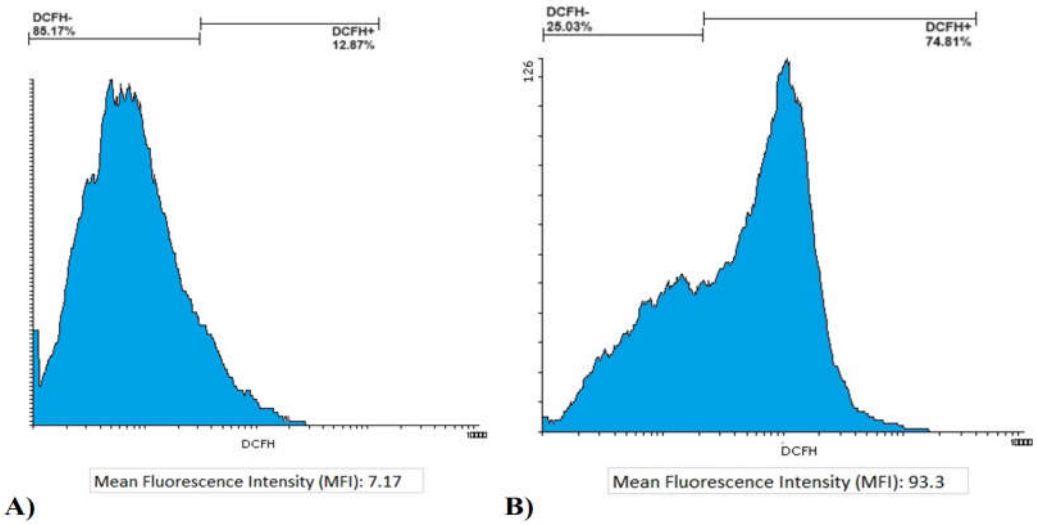

Fig. 10. Intracellular ROS levels in HT-116 cells measured by H_2DCF fluorescence intensity: A) Control cells showing 12.87% $DCFH^+$ population with mean fluorescence intensity (MFI) of 7.17; B) Fe_3O_4@Glu-HA-NAR NPs-treated cells showing 74.81% $DCFH^+$ population with MFI of 93.3, indicating a 13.0-fold increase in intracellular ROS levels following treatment with the nanoparticles.

Discussion

Nanotechnology-assisted drug delivery offers several advantages, including improved drug stability and biocompatibility, enhanced bioavailability, and increased therapeutic efficiency. Therefore, using NPs as drug carriers in cancer chemotherapy has gained attention. Targeting cancer cells using functionalized NPs can enhance drug accumulation in target sites and decrease off-target drug release, leading to improved efficiency and reduced side effects of chemotherapy (Haleem *et al.,* 2023). The current work aimed to characterize the anticancer potential of Fe_3O_4@Glu-HA-NAR NPs against colon cancer cells.

The physicochemical characterization collectively confirmed the successful fabrication of the Fe_3O_4@Glu-HA-NAR nanocomposite. FTIR analysis verified the successful surface functionalization of Fe_3O_4 nanoparticles with glucose, hyaluronic acid, and NAR, while XRD confirmed that the crystalline structure of the Fe_3O_4 core was preserved after surface modification. FESEM images demonstrated that the nanoparticles possessed a nearly spherical morphology. It should be noted that the apparent agglomeration observed in the SEM images is mainly attributable to sample drying during SEM preparation and does not necessarily represent the dispersion state of the nanoparticles in aqueous suspension. In contrast, DLS provides a more representative assessment of particle size distribution under dispersion conditions. The obtained PDI value indicates a moderate particle size distribution in suspension, supporting the successful formation of the nanoparticle formulation. Furthermore, the high negative zeta potential suggests good colloidal stability of the nanoparticles, which is favorable for biological applications.

To further evaluate the contribution of nanoparticle formulation to the observed anticancer activity, the cytotoxic effects of Fe_3O_4@Glu-HA-NAR nanoparticles were compared with those of free NAR. The MTT assay demonstrated that Fe_3O_4@Glu-HA-NAR nanoparticles exhibited greater antiproliferative activity than free NAR, as evidenced by a lower IC_{50} value (42.63 vs. 64.62 µg/mL). This improvement is likely attributable to enhanced cellular uptake, increased stability of NAR after nanoparticle conjugation, prolonged intracellular retention, and HA-mediated targeting through CD44 receptors, which are overexpressed in colorectal cancer cells (Phatak *et al.*, 2023). Collectively, these findings indicate that the HA-functionalized iron oxide nanocarrier effectively enhances the therapeutic efficacy of NAR compared with the free compound, supporting the potential of this targeted delivery system for colorectal cancer therapy.

The antiproliferative potential of Fe_3O_4@Glu-HA-NAR NPs seems to be mainly related to their NAR content. Several studies indicated the multifunctional cytotoxic effects of NAR. The major underlying anticancer mechanisms of NAR include upregulation of the expression of anticancer mediators such as *BAX*, *caspases*, *p53,* and *p21*; inducing cell cycle arrest, modulation of cancer development markers such as PI3K/Akt/mTOR and NF-κB, and apoptosis induction (Noman *et al.,* 2025). Lozano-Herrera *et al.* (2022) reported that NAR exerts antiproliferative effects on human colorectal cancer cells through promoting expression of the phosphatase and Tensin homolog (PTEN) and *CASP-9*. Moreover, it promoted intrinsic apoptosis through modulation of the genes associated with P53 signaling pathways. Similar findings were also reported by *Zeya et al.,* (2022), who investigated the apoptosis induction potential of NAR in colon cancer cell lines, HCT-116 and SW480. They found that NAR has concentration-dependent cytotoxicity toward colon cancer cell lines, causing DNA fragmentation, chromatin condensation, cell cycle arrest at the G0/G1 phase, and cell apoptosis induction. Similar to their findings, we observed that the synthesized NPs can promote apoptosis induction in the colon cancer cells and cause cell cycle arrest. In addition, they found that NAR induced the pro-apoptotic genes, including *CASP-3*, *CASP-8* and *CASP-9*, indicating triggering the intrinsic and extrinsic apoptosis in the exposed cells. Consistent with these findings, we observed an overexpression of the *CASP-8* gene and increased cell apoptosis/necrosis in cancer cells treated with Fe_3O_4@Glu-HA-NAR NPs, indicating the underlying antiproliferative potential of the synthesized NPs in colon cancer cells.

In agreement with our finding, Song *et al.* (2016) reported that treatment of various colorectal cancer cell lines with NAR significantly decreased cell viability and causes a dose-dependent overexpression of the Activating Transcription Factor-3 (ATF-3) at mRNA and protein levels. They found that ATF-3 is a main molecular target of NAR in colorectal cancer cells and ATF-3 overexpression contributes to p38 activation in the NAR-treated cells. It has been demonstrated that the p38 signaling pathway is involved in the induction of ATF-3 by stress signals. Lu *et al.* (2007) found that p38 is necessary for oxidative stress mediated activation of the ATF-3 and ATF-3 is functionally important to mediate the pro-apoptotic effects of p38.

Quantification of the ROS levels showed that exposure of HT-116 cells to the synthesized NPs intensified ROS generation, exhibiting the role of oxidative stress induction in the exposed cells. As described above, ROS generation can induce p38-related proapoptotic pathways in the treated cells, resulting in cell cycle arrest, caspase induction, and increased apoptosis. In addition, ROS generation can cause damage to various cell components, including cell membranes and DNA, leading to disruption of normal cellular functions (Zhao *et al.,* 2023). It has been demonstrated that NAR inhibits the viability of human cancer cells through a significant increase in intracellular ROS levels, leading to endoplasmic reticulum (ER) stress-mediated apoptosis, cell cycle arrest by inhibiting cyclin B1 and cyclin-dependent kinase 1 and upregulation of the *p21* gene (Lee *et al.,* 2022). Furthermore, Zhang *et al.* (2023) reported a considerable accumulation of ROS in human cancer cells following exposure to NAR, resulting in mitochondrial membrane potential loss, DNA fragmentation and caspase activation, leading to reduced cell viability and apoptosis induction. The ROS-mediated cytotoxic effects of NAR on human cancer cells have also been documented by Chang *et al.* (2024). They found that NAR induced cell cycle arrest at the G2/M phase, triggered autophagy by mediating ROS generation, thereby activating AMP-activated protein kinase (AMPK) signaling. In addition, supplementation with ROS scavengers considerably relieved the cytotoxic potential of NAR in cancer cells, thereby indicating the role of oxidative stress in the anticancer effects of NAR, which is consistent with our work.

The marked increase in intracellular ROS levels following treatment with Fe_3O_4@Glu-HA-NAR nanoparticles suggests that oxidative stress is a major mechanism underlying the observed apoptosis and cell cycle arrest. Excessive ROS can damage cellular macromolecules, including DNA, proteins, and lipids, thereby activating stress-responsive signaling pathways and

apoptotic cascades (Wang *et al.*, 2023). While transient ROS generation can function as a signaling mechanism, sustained or excessive ROS production may trigger additional cellular responses, including autophagy, senescence, or adaptive antioxidant defense mechanisms, depending on the intensity and duration of oxidative stress (Pantelis *et al.*, 2023). In the present study, the pronounced ROS elevation was associated with apoptosis induction and cell cycle arrest; however, investigation of other ROS-mediated cellular responses was beyond the scope of this work and warrants further study.

Flow cytometric analysis demonstrated that Fe_3O_4@Glu-HA-NAR nanoparticles markedly enhanced intracellular ROS generation, as evidenced by both a substantial increase in the percentage of DCFH-positive cells and an approximately 13-fold increase in MIF. The increased proportion of DCFH-positive cells indicates that oxidative stress was induced in the majority of the treated cell population, whereas the elevated MFI reflects a marked increase in the intracellular ROS level within individual ROS-positive cells. Together, these findings demonstrate that the nanoparticles induced widespread and intense oxidative stress, which may contribute to the activation of apoptotic signaling pathways observed in this study.

Although an increased PI-positive cell population was observed after 24 h of treatment, this finding should not be interpreted as evidence of primary necrotic cell death. Considering the significant upregulation of *CASP-8* expression, increased ROS production, and Annexin V positivity, apoptosis appears to be the predominant mechanism of cell death. The PI-positive population is therefore more likely to represent secondary necrosis, reflecting the progression of apoptotic cells to a late stage characterized by loss of plasma membrane integrity (Demchenko, 2013).

The anticancer potential of NAR in colon cancer cells can also be related to the inhibition of RAS activation. Colon cancer in humans is strongly associated with mutational activation of RAS oncoproteins that stimulate their downstream effectors, including PI3K/AKT/mTOR1, Raf-1/MEK/ERK, and JNK pathways, causing abnormal cell proliferation and increased tumor aggressiveness. It has been found that some NAR derivatives can induce cell growth inhibition and autophagy pathways in colon cancer cells, though the inhibition of RAS activation. This finding can be an underlying mechanism for the stronger cytotoxicity of Fe_3O_4@Glu-HA-NAR NPs in colon cancer cell line than in normal cells (Zhao *et al.,* 2016). However, the selective anticancer potential of Fe_3O_4@Glu-HA-NAR NPs against colon cancer cells seems to be mainly related to HA-assisted targeting of cancer cells. HA plays several roles in cell proliferation and physiological processes. Due to the higher expression of HA receptors on the surface of cancer cells compared to normal cells, Fe_3O_4@Glu-HA-NAR NPs can target them more efficiently, causing more potent inhibition of cancer cells (Michalczyk *et al.,* 2022; Dosio *et al.,* 2016; Saiprasad *et al.,* 2024; Heydari *et al.*, 2025).

The improved anticancer potential of anticancer through targeting of HA receptors has been reported in the literature. Parashar *et al.* (2018) reported the superior cytotoxic effect and active targeting of lung cancer cells by NAR-loaded polycaprolactone nanoparticles decorated with HA, which caused enhanced cell cycle arrest and effective growth inhibition of cancer cells. Targeting colon cancer cells through HA receptors has also been reported, which is in agreement with our work. Pan *et al.* (2021) reported that HA-doxorubicin nanoparticles efficiently target colon cancer tumors and reduce intestinal drug accumulation in a mouse model, resulting in more efficient and safer treatment of colon tumors.

In addition, HA receptor targeting of colon cancer cells by HA-coated PLGA-polysarcosine (PSAR) coupled with sorafenib tosylate (SF) nanoparticles demonstrated superior drug delivery and cytotoxicity against colorectal cancer cells and improved biocompatibility. In agreement with our work, they reported the improved drug delivery to cancer cells through targeting HA receptors (Phatak *et al.,* 2023). Although the loading efficiency of NAR was determined, the drug loading capacity and in vitro release kinetics were not evaluated in this study. Future studies should investigate these parameters to further characterize the

pharmaceutical performance of the developed nanocarrier.

Conclusion

In this work, the anticancer potential of Fe_3O_4@Glu-HA-NAR NPs in the colon cancer cell line was characterized. This study demonstrated that Fe_3O_4@Glu-HA-NAR NPs cause superior and efficient inhibition of cancer cells than normal ones, causing considerable elevation of intercellular ROS levels, leading to cell cycle blockage at the S and G2/M phases, remarkable increase in cell apoptosis/necrosis, nuclear damage and significant upregulation of the *CASP-8* gene. These findings suggest the promising and efficient targeting of colon cancer cells by Fe_3O_4@Glu-HA-NAR NPs, which can be considered in chemotherapy approaches after pharmacokinetic and *in vivo* characterizations.

Conflict of interests

The authors have no conflicts of interest to declare.

References

Ahmadzadeh Chaleshtori, M. A., Salehzadeh, A., & Peymani, M. (2025). Identification of oncogenes associated with colorectal cancer mortality and the effect of cinnamon-conjugated magnetic nanoparticles on their expression. *Scientific Reports*, 15(1), 17467. https://doi.org/10.1038/s41598-025-02189-3

Chang, T. M., Chi, M. C., Chiang, Y. C., Lin, C. M., Fang, M. L., Lee, C. W., Liu, J. F., & Kou, Y. R. (2024). Promotion of ROS-mediated apoptosis, G2/M arrest, and autophagy by naringenin in non-small cell lung cancer. *International Journal of Biological Sciences*, 20(3), 1093. https://doi.org/10.7150/ijbs.85443

De Luna, F. C. F., Ferreira, W. A. S., Casseb, S. M. M., & De Oliveira, E. H. C. (2023). Anticancer potential of flavonoids: An overview with an emphasis on tangeretin. *Pharmaceuticals*, 16(9), 1229. https://doi.org/10.3390/ph16091229

De Souza, W. R., Quevedo, B. V., Garcia, P. S., da Silva, L. C. S. C., Komatsu, D., & Duek, E. A. R. (2025). Synthesis and physical–chemical characterization of chitosan grafted with hyaluronic acid as potential application in biomaterials. *Polymer Bulletin*, 82, 1915-1933. https://doi.org/10.1007/s00289-024-05595-1

Demchenko, A. P. (2013). Beyond annexin V: Fluorescence response of cellular membranes to apoptosis. *Cytotechnology*, 65(2), 157-172. https://doi.org/10.1007/s10616-012-9481-y

Dosio, F., Arpicco, S., Stella, B., & Fattal, E. (2016). Hyaluronic acid for anticancer drug and nucleic acid delivery. *Advanced Drug Delivery Reviews*, 97, 204-236. https://doi.org/10.1016/j.addr.2015.11.011

Esfahani, M. A., Salehzadeh, A., & Ghobeh, M. (2024). Anti-proliferative activity of magnetic iron oxide nanoparticles functionalized glucose and conjugated cinnamon against gastric cell line. *BioNanoScience*, 14(5), 5069-5079. https://doi.org/10.1007/s12668-024-01562-2

Fu, C. P., Cai, X. Y., Chen, S. L., Yu, H. W., Fang, Y., Feng, X. C., Zhang, L. M., & Li, C. Y. (2023). Hyaluronic acid-based nanocarriers for anticancer drug delivery. *Polymers*, 15(10), 2317. https://doi.org/10.3390/polym15102317

Gambhir, R. P., Rohiwal, S. S., & Tiwari, A. P. (2022). Multifunctional surface functionalized magnetic iron oxide nanoparticles for biomedical applications: A review. *Applied Surface Science Advances*, 11, 100303. https://doi.org/10.1016/j.apsadv.2022.100303

Haleem, A., Javaid, M., Singh, R. P., Rab, S., & Suman, R., (2023). Applications of nanotechnology in medical field: A brief review. *Global Health Journal*, 7(2), 70-77. https://doi.org/10.1016/j.glohj.2023.02.008

Hosseinkhah, M., Ghasemian, R., Shokrollahi, F., Mojdehi, S. R., Noveiri, M. J. S., Hedayati, M., Rezaei, M., & Salehzadeh, A. (2022). Cytotoxic potential of nickel oxide nanoparticles functionalized with glutamic acid and conjugated with thiosemicarbazide (NiO@Glu/TSC) against human gastric cancer cells. *Journal of Cluster Science*, 33(5), 2045-2053. https://doi.org/10.1007/s10876-021-02124-2

Heydari, M., Colagar, A. H., Sabour, D., & Khorasani, H. R. (2024). Evidence of Urtica dioica agglutinin's antiproliferative and anti-migratory potentials on the hyaluronic acid-overexpressing prostate cancer cells. *Planta*

Medica, 90(10), 774-784. https://doi.org/10.1055/a-2324-2250

Heydari, M., Colagar, A. H., & Sabour, D. (2025). Anti-proliferative and anti-migratory effects of Urtica dioica agglutinin loaded chitosan nanoparticles with hyaluronic acid coating on the CD44-overexpressing prostate cancer cells. *International Journal of Environmental Health Research*, 35(10), 2929-2943. https://doi.org/10.1080/09603123.2025.2465877

Jia, Y., Chen, S., Wang, C., Sun, T., & Yang, L. (2022). Hyaluronic acid-based nano drug delivery systems for breast cancer treatment: Recent advances. *Frontiers in Bioengineering and Biotechnology*, 10, 990145. https://doi.org/10.3389/fbioe.2022.990145

Kazemzadeh, D., Salehzadeh, A., Shariati, S., & Shandiz, S. A. S. (2026). Hyaluronic acid/kaempferol-functionalized Fe_3O_4 nanoparticles promote ROS-associated apoptosis and modulate caspase-8/BCRT1 axis in triple-negative breast cancer. *Scientific Reports*, 16, 21797. https://doi.org/10.1038/s41598-026-50528-9

Kumari, R., Saini, A. K., Kumar, A., & Saini, R. V. (2020). Apoptosis induction in lung and prostate cancer cells through silver nanoparticles synthesized from Pinus roxburghii bioactive fraction. *Journal of Biological Inorganic Chemistry*, 25(1), 23-37. https://doi.org/10.1007/s00775-019-01729-3

Lee, H. C., Huang, K. H., Chi, M. C., Lee, K. H., Peng, K. T., Fang, M.L., Chiang, Y. C., & Liu, J. F. (2022). Naringenin induces ROS-mediated ER stress, autophagy, and apoptosis in human osteosarcoma cell lines. *Molecules*, 27(2), 373. https://doi.org/10.3390/molecules27020373

Lozano-Herrera, S. J., Luna-Barcenas, G., Guevara-Gonzalez, R. G., Campos-Vega, R., Solis-Sainz, J. C., Hernandez-Puga, A. G., & Vergara-Castaneda, H. A. (2022). Fermentation extract of naringenin increases the expression of estrogenic receptor β and modulates genes related to the p53 signalling pathway, miR-200c and miR-141 in human colon cancer cells exposed to BPA. *Molecules*, 27(19), 6588. https://doi.org/10.3390/molecules27196588

Lu, D., Chen, J., & Hai, T. (2007). The regulation of ATF3 gene expression by mitogen-activated protein kinases. *Biochemical Journal*, 401(2), 559-567. https://doi.org/10.1042/BJ20061081

Michalczyk, M., Humeniuk, E., Adamczuk, G., & Korga-Plewko, A. (2022). Hyaluronic acid as a modern approach in anticancer therapy-review. *International Journal of Molecular Sciences*, 24(1), 103. https://doi.org/10.3390/ijms24010103

Najafipour, I., Emami, N., Sadeh, P., Amoli, A., Mosleh-Shirazi, S., Amani, A. M., Kamyab, H., Chelliapan, S., Kasaee, S. R., & Vafa, E. (2025). Synthesis of Fe3O4@MIL-101-OH/Chitosan for adsorption and release of doxorubicin. *Polymer Testing*, 142, 108659. https://doi.org/10.1016/j.polymertesting.2024.108659

Noman, A.M., Sultan, M.T., Raza, H., Imran, M., Hussain, M., Mujtaba, A., Mostafa, E.M., Ghoneim, M.M., Selim, S., Al Jaouni, S.K., Abdelgawad, M.A., Yehuala, T. F., Alsagaby, S., & AlAbdulmonem, W. (2025). An updated review of the anticancer mechanisms and therapeutic potential of naringenin. *Food Science & Nutrition*, 13(7), e70626. https://doi.org/10.1002/fsn3.70626

Oki, E., Ando, K., Taniguchi, H., Yoshino, T., & Mori, M. (2022). Sustainable clinical development of adjuvant chemotherapy for colon cancer. *Annals of Gastroenterological Surgery*, 6(1), 37-45. https://doi.org/10.1002/ags3.12503

Pan, D. C., Krishnan, V., Salinas, A. K., Kim, J., Sun, T., Ravid, S., Peng, K., Wu, D., Nurunnabi, M., Nelson, J. A., Niziolek, Z., Guo, J., & Mitragotri, S. (2021). Hyaluronic acid–doxorubicin nanoparticles for targeted treatment of colorectal cancer. *Bioengineering & Translational Medicine*, 6(1), e10166. https://doi.org/10.1002/btm2.10166

Pantelis, P., Theocharous, G., Lagopati, N., Veroutis, D., Thanos, D. F., Lampoglou, G. P., Pippa, N., Gatou, M. A., Tremi, I., Papaspyropoulos, A., Kyrodimos, E., Pavlatou, E. A., Gazouli, M., Konstantinos Evangelou, K., & Gorgoulis, V. G. (2023). The dual role of oxidative-stress-induced autophagy in cellular senescence: Comprehension and therapeutic approaches. *Antioxidants*, 12(1), 169. https://doi.org/10.3390/antiox12010169

Parashar, P., Rathor, M., Dwivedi, M., & Saraf, S. A. (2018). Hyaluronic acid decorated naringenin nanoparticles: Appraisal of chemopreventive and curative potential for lung cancer. *Pharmaceutics*, 10(1), 33. https://doi.org/10.3390/pharmaceutics10010033

Pfaffl, M. W. (2001). A new mathematical model for relative quantification in real-time RT-PCR. *Nucleic Acids Research*, 29(9), e45. https://doi.org/10.1093/nar/29.9.e45

Phatak, N., Bhattacharya, S., Shah, D., Manthalkar, L., Sreelaya, P., & Jain, A. (2023). CD44 targeted delivery of hyaluronic acid-coated polymeric nanoparticles against colorectal cancer. *Nanomedicine*, 18(23), 1613-1634. https://doi.org/10.2217/nnm-2023-0145

Ramezani, T., Nabiuni, M., Baharara, J., Parivar, K., & Namvar, F. (2019). Sensitization of resistance ovarian cancer cells to cisplatin by biogenic synthesized silver nanoparticles through p53 activation. *Iranian Journal of Pharmaceutical Research*, 18(1), 222-231. https://doi.org/10.22037/ijpr.2019.2358

Rauf, A., Shariati, M. A., Imran, M., Bashir, K., Khan, S. A., Mitra, S., Emran, T. B., Badalova, K., Uddin, M. S., Mubarak, M. S., Aljohani, A. S., Alhumaydhi, F. A., Derkho, M., Korpayev, S., & Zengin, G. (2022). Comprehensive review on naringenin and naringin polyphenols as a potent anticancer agent. *Environmental Science and Pollution Research*, 29(21), 31025-31041. https://doi.org/10.1007/s11356-022-18754-6

Saiprasad, G., Chitra, P., Manikandan, R., Koodalingam, A., & Sudhandiran, G. (2024). Hesperetin regulates PI3K/Akt and mTOR pathways to exhibit its antiproliferative effect against colon cancer cells. *Biotechnic & Histochemistry*, 99(6), 287–304. https://doi.org/10.1080/10520295.2024.2382764

Sharma, T., Gorivale, S., & Bhandari, P. (2024). Targeted drug delivery in cancer using nanomaterials: Advances and challenges. *Journal of Nanoparticle Research*, 26(6), 127. https://doi.org/10.1007/s11051-024-06023-1

Song, H. M., Park, G. H., Eo, H. J., & Jeong, J. B. (2016). Naringenin-mediated ATF3 expression contributes to apoptosis in human colon cancer. *Biomolecules & Therapeutics*, 24(2), 140. https://doi.org/10.4062/biomolther.2015.109

Stabrauskiene, J., Kopustinskiene, D. M., Lazauskas, R., & Bernatoniene, J. (2022). Naringin and naringenin: Their mechanisms of action and the potential anticancer activities. *Biomedicines*, 10(7), 1686. https://doi.org/10.3390/biomedicines10071686

Stanicki, D., Vangijzegem, T., Ternad, I., & Laurent, S. (2022). An update on the applications and characteristics of magnetic iron oxide nanoparticles for drug delivery. *Expert Opinion on Drug Delivery*, 19(3), 321-335. https://doi.org/10.1080/17425247.2022.2047020

Sung, H., Ferlay, J., Siegel, R. L., Laversanne, M., Soerjomataram, I., Jemal, A., Bray, F. (2021). Global cancer statistics 2020: GLOBOCAN estimates of incidence and mortality worldwide for 36 cancers in 185 countries. *CA: A Cancer Journal for Clinicians*, 71(3), 209-249. https://doi.org/10.3322/caac.21660

Wang, B., Wang, Y., Zhang, J., Hu, C., Jiang, J., Li, Y., & Peng, Z. (2023). ROS-induced lipid peroxidation modulates cell death outcome: Mechanisms behind apoptosis, autophagy, and ferroptosis. *Archives of Toxicology*, 97(6), 1439-1451. https://doi.org/10.1007/s00204-023-03476-6

Wang, D., Zhou, Y., Hua, L., Hu, M., Zhu, N., Liu, Y., & Zhou, Y. (2024). The role of the natural compound naringenin in AMPK-mitochondria modulation and colorectal cancer inhibition. *Phytomedicine*, 131, 155786. https://doi.org/10.1016/j.phymed.2024.155786

Xie, Y., Zhou, J., Zhang, B., Zhang, L., Yang, D., Yang, S., Fang, L., Lu, Y., & Du, G. (2024). Quality control of naringenin-carbamazepine drug-drug cocrystal: Quantitative analytical method construction of ATR-FTIR and Raman combined with chemometrics. *Microchemical Journal*, 202, 110774. https://doi.org/10.1016/j.microc.2024.110774

Yilmaz, M. D., Ozsamur, N. G., & Erbas-Cakmak, S. (2024). Catalytic investigation of hyaluronic acid-stabilized Ag nanoparticles as non-toxic nanocatalysts in the oxidation of morin. *New Journal of Chemistry*, 48(5), 2341-2347. https://doi.org/10.1039/D3NJ05411J

Zamanian, M. Y., Golmohammadi, M., Abdullaev, B., Garcia, M. O., Alazbjee, A. A. A., Kumar, A., Mohaamed, S. S., Hussien, B. M., Khalaj, F., Hodaei, S. M., Shirsalimi, N., & Moriasi, G. (2024). A narrative review on therapeutic potential of naringenin in colorectal cancer: Focusing on molecular and biochemical processes. *Cell Biochemistry and Function*, 42(3), e4011. https://doi.org/10.1002/cbf.4011

Zhang, M., Lai, J., Wu, Q., Lai, J., Su, J., Zhu, B., & Li, Y. (2023). Naringenin induces HepG2 cell apoptosis via ROS-mediated JAK-2/STAT-3 signaling pathways. *Molecules*, 28(11), 4506. https://doi.org/10.3390/molecules28114506

Zhao, Y., Fan, D., Ru, B., Cheng, K.W., Hu, S., Zhang, J., Li, E.T., & Wang, M. (2016). 6-C-(E-phenylethenyl) naringenin induces cell growth inhibition and cytoprotective autophagy in colon cancer cells. *European Journal of Cancer*, 68, 38-50. https://doi.org/10.1016/j.ejca.2016.09.001

Zhao, Y., Ye, X., Xiong, Z., Ihsan, A., Ares, I., Martínez, M., Lopez-Torres, B., Martínez-Larrañaga, M.R., Anadón, A., Wang, X., & Martínez, M.A. (2023). Cancer metabolism: the role of ROS in DNA damage and induction of apoptosis in cancer cells. *Metabolites*, 13(7), 796. https://doi.org/10.3390/metabo13070796

Zeya, B., Nafees, S., Imtiyaz, K., Uroog, L., Fakhri, K.U., & Rizvi, M.M.A. (2022). Diosmin in combination with naringenin enhances apoptosis in colon cancer cells. *Oncology Reports*, 47(1), 4. https://doi.org/10.3892/or.2021.8215